Nucleic Acids Research Advance Access published September 3, 2015

Nucleic Acids Research, 2015 **1**
doi: 10.1093/nar/gkv866

Nano-mechanical measurements of protein-DNA interactions with a silicon nitride pulley

Min Ju Shon and Adam E. Cohen*

Department of Chemistry and Chemical Biology and Department of Physics, Harvard University and Howard Hughes Medical Institute, Cambridge, MA 02138, USA

Received April 17, 2014; Revised July 26, 2015; Accepted August 15, 2015

ABSTRACT

Proteins adhere to DNA at locations and with strengths that depend on the protein conformation, the underlying DNA sequence and the ionic content of the solution. A facile technique to probe the positions and strengths of protein-DNA binding would aid in understanding these important interactions. Here, we describe a 'DNA pulley' for position-resolved nano-mechanical measurements of protein-DNA interactions. A molecule of λ DNA is tethered by one end to a glass surface, and by the other end to a magnetic bead. The DNA is stretched horizontally by a magnet, and a nanoscale knife made of silicon nitride is manipulated to contact, bend and scan along the DNA. The mechanical profile of the DNA at the contact with the knife is probed via nanometer-precision optical tracking of the magnetic bead. This system enables detection of protein bumps on the DNA and localization of their binding sites. We study theoretically the technical requirements to detect mechanical heterogeneities in the DNA itself.

INTRODUCTION

Mechanics of protein-DNA interactions

Site-specific protein-DNA interactions are critical for DNA replication, packaging, transcription and repair. Bulk measurements via chromatin immunoprecipitation followed by sequencing (ChIP-seq) provide genome-wide information on binding sites, (1) but do not provide thermodynamic or kinetic information, nor probe single-molecule variations. Optical profiling techniques can follow the motion of proteins along single stretched strands of DNA (2), or along curtains comprised of many aligned molecules (3). These techniques require fluorescent labeling and encounter the challenges with photostability and spatial resolution common to all fluorescence measurements. High-resolution AFM can identify bound proteins (4) and putative kinks (5) in DNA, but these measurements might be confounded by interactions with the surface. Solid state nanopores have been used to detect the presence of proteins bound to DNA through occlusion of the nanopore by the protein (6), and to locate proteins on the DNA by controlling passage of the DNA through the pore with optical tweezers (7).

A clever recent technique used one DNA molecule held in a dual-beam optical trap to scan against another molecule stretched by magnetic tweezers (8,9). By using a flexible DNA strand as the probe, this technique experiences ambiguity in the exact contact location between the probe and target strands of DNA.

We developed a DNA pulley system (without a wheel) in which a nanofabricated knife scans along a magnetically stretched molecule of dsDNA. This approach uses a rigid and chemically well-defined surface as the probe, and uses a very simple optical setup. Single molecules of dsDNA can be probed along their sequence with nanometer precision for measurement times >1 h. The DNA pulley system gave clear signatures of proteins bound to the DNA, but did not detect increases in flexibility associated with single-stranded nicks. We model the effect of a perfectly flexible joint theoretically, and discuss the signal-to-noise requirements of detecting nicks, joints, and sequence-dependent changes in bending modulus.

MATERIALS AND METHODS

DNA pulley construct

Molecules of λ phage DNA (48.5 kb) were attached on one end to the exterior of a square glass capillary (1 mm I.D., Friedrich & Dimmock, BMC-1-15-50) via a digoxigenin anti-dig linker, and on the other end to a superparamagnetic bead (1 μm diameter, Life Technologies, MyOne^{TM} Streptavidin C1) via a biotin-streptavidin linker. This tethering protocol (details in Supplementary Data) was adapted from references (10–12). The purpose of the capillary was to allow the DNA to be stretched parallel to the focal plane of the microscope without concern about interactions between the bead and the coverslip. Movie S1 shows displacement of the tethered beads indicating stretching of the DNA in the

*To whom correspondence should be addressed. Tel: +1 617 496 9466; Email: cohen@chemistry.harvard.edu
Present address: Min Ju Shon, Department of Physics, KAIST, Daejeon 305-701, South Korea.

presence of a magnetic field gradient generated by a permanent magnet.

At a stretching force of 1 pN, the WLC model predicts a displacement of 13.9 μm for single-tethered beads. For double-tethered beads, the greatest displacement occurs when the tension is shared equally between the strands, implying a displacement of 12.9 μm or less, depending upon the locations of the DNA attachment points. Beads displaced by less than the population mode were visually apparent and were not used in experiments.

Silicon nitride knife fabrication

A 55 nm film of low-stress silicon nitride was deposited on the clean (100) face of a silicon wafer via chemical vapor deposition (Supplementary Data). The film thickness was measured by ellipsometry. The wafer was manually cleaved into slivers 4 mm × 15 mm. A silicon nitride overhang (the blade) was formed by a selective Si etch (KOH, 30% w/v, 75°C, 20–30 min). The slivers were then carefully washed in distilled water and air dried. Examination of the edges under a dissecting microscope showed small free-standing films of silicon nitride protruding past the etched edges. Examination in a scanning electron microscope showed a smooth blade, free of cracks or grooves, with a thickness of 55 nm, an overhang length of typically 10–20 μm (Figure 1D–E), and a length along its edge of 1–2 mm. A NdFeB magnet (1/16' cube, K&J Magnetics, B111) was glued to the back face of the silicon sliver to provide the stretching force.

Measurement setup

The DNA-coated capillary and the nitride blade were mounted in a sample chamber as shown in Figure 1A and F. The capillary and magnetically stretched DNA both lay in the focal plane of an inverted microscope. The blade was aligned with its face in the y-z plane, parallel to the surface of the capillary (see Figure 1A and F for coordinate system), and its edge along the z-axis, perpendicular to the image plane of the microscope. A manual micromanipulator was used to position the blade at $x \approx 2$ μm from the face of the capillary and $y \approx -2$ μm from the strand of DNA. The tip of the blade was positioned at $z \approx -5$ μm below the DNA to prevent the DNA from unhooking during scanning. Thereafter the blade was kept stationary and the capillary carrying the DNA was positioned via a piezoelectric nanopositioning stage (Mad City Labs, Nano-LP100). Scans were along the y-axis, typically 12–14 μm in length, at 1 μm/s. A transmitted-light image of the bead was recorded on a CCD camera and used to track the location of the bead with nanometer precision using a fast tracking algorithm (13). The entire apparatus was enclosed in a box to block air currents and thermal fluctuations, and was mounted on a vibration isolation table.

RESULTS AND DISCUSSION

Calibration of DNA pulley

The DNA pulley system depends critically on the ability to track the motion of the bead with high precision. Jitter in the measured bead locations can arise from optical or electronic noise in the images; from drift or vibrations of the sample chamber; or from Brownian fluctuations of the bead itself. We characterized each contribution to the noise in turn. To quantify the contribution from measurement noise (optical and electronic) we simultaneously tracked two beads affixed to a dry coverslip. Measurement noise manifested as apparent fluctuations in the vector joining the beads. These fluctuations had an r.m.s. amplitude of 0.19 nm in a 1 Hz bandwidth, implying a single-bead tracking precision of 0.13 nm along each axis. The stage introduced an additional common-mode position noise of 2 nm along each axis, and had a minimum step size of 5 nm. The system had long-term thermal drift of ~1 nm/min. A detailed analysis of the temporal structure of the mechanical drift is in Supplementary Figure S5. Steps in the piezo position of 5 nm were clearly resolved (Figure 2A).

When a bead was held by its DNA tether, its fluctuations in position were significantly larger than the measurement noise. The fluctuations formed an ellipse, with principal axes $\hat{r}$ parallel and $\hat{w}$ perpendicular to the direction of DNA stretching (Figure 2B). The standard deviations of the fluctuations were $\sigma_r = 32$ nm and $\sigma_w = 89$ nm. We calculated the autocorrelation function of the position fluctuations along each axis, and fit to an exponential decay, with decay times $\tau_r = 10$ ms and $\tau_w = 68$ ms (Figure 2C). These parameters set the fundamental limits on how precisely the bead's center of mass can be localized. If one integrates for a time t, the r.m.s. uncertainty in the center of mass is $\sigma_{\text{meas}} = \sigma_{\text{therm}}\sqrt{\tau/t}$, where σ_{therm} is the width of the Brownian distribution (equal σ_r or σ_w).

We estimated the stretching tension in the DNA (in the absence of the blade) from the relaxation time of the thermal fluctuations (14). From the relaxation time and the estimated Stokes drag on the bead we inferred a spring constant (Supplementary Eq. 2). From the WLC force-extension curve (Supplementary Eq. 3) we then inferred a force (Supplementary Figure S7). In these calibrations, we accounted explicitly for blurring due to the finite exposure time of the camera (Supplementary Figure S6D). These estimates implied a mean tension of 1.0 pN, which stretched the DNA to 85% of its 16.2 μm contour length. An uncertainty of ±5 ms in the relaxation time led to an uncertainty of ±0.25 pN in the force. The discussion below does not depend on the precise value of the force.

During an experiment, the bead-magnet distance varied by ($\delta R \sim 10$ μm) while the mean distance was $R \sim 1$ mm. The force, F, on the bead was proportional to the gradient of the magnetic field. For a dipolar $F \propto 1/R^4$. Thus the fractional variation in the force on the bead was approximately $4\,\delta R/R \sim 4\%$. We did not include these variations in tension in our analysis. When the DNA slid smoothly over the pulley, the tension was uniform throughout the strand. When the motion stalled, the tension between the blade and attachment point could be greater or less than the magnetic tension, depending upon the direction of motion.

Operation and geometry of the pulley

Figure 3 shows a typical bead trajectory, Supplementary Movie S2 shows an animation, and Supplementary Movies

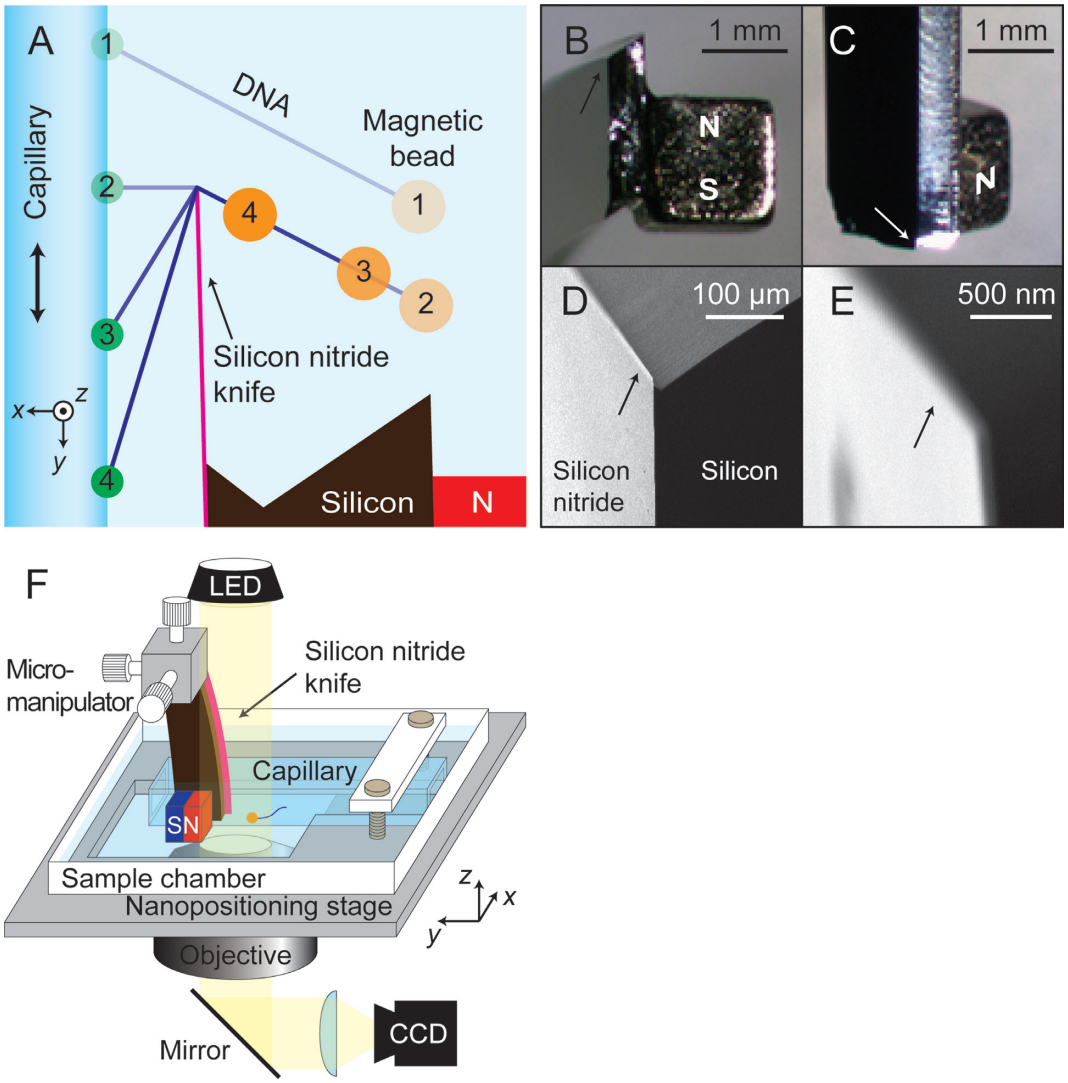

Figure 1. DNA pulley system. (**A**) Schematic of the experiment. The silicon nitride knife is held fixed, while a square capillary carrying a magnetically stretched molecule of DNA on its exterior is brought toward the knife edge (1) until the DNA makes contact with the blade (2). Further movement of the capillary drags the DNA over the blade edge in a pulley fashion (3,4). (**B**–**E**) Images of the blade and magnet. Arrows indicate location of the blade. (**B** and **C**) Stereomicroscope images of a silicon wafer supporting a silicon nitride blade (not visible) on one face and a permanent magnet glued to the opposite face. (**D** and **E**) Scanning electron microscope images of the silicon nitride blade. The blade protrudes 10–20 μm from the silicon wafer and has a thickness of 55 nm. (**F**) Experimental setup. The capillary carrying the DNA is mounted rigidly in a sample chamber, which is held by a piezoelectric positioning stage. Coarse approach of the blade to the DNA is achieved via a micromanipulator; the blade is then held fixed while the capillary and sample chamber are moved by the piezoelectric stage.

S3 and S4 show videos of the scanning process. Before the DNA touched blade, the motion of the bead followed the motion of the capillary parallel to the *y*-axis. Following contact, the bead initially moved away from the blade along the *r*-axis and then moved toward the blade. The motion of the bead revealed the orientation of the *r*-axis, typically oriented at $\theta_F \approx 45^\circ$ below the *x*-axis.

The bead trajectory can be predicted by solving the geometry of the pulley system. The parameters are the piezo movement along the *y*-axis, *P*, the separation of the blade from the capillary, *d*, and the total contour length of the DNA, l_0, assumed to remain constant throughout a scan. We define $P = 0$ when the line joining the surface attachment point and the knife edge is purely along the *x*-axis. The radial displacement of the bead, *r*, is given by:

$$r = l_0 - \sqrt{p^2 + d^2}. \quad (1)$$

The transverse displacement, *w*, is zero as long as the DNA is in contact with the blade. Figure 3 shows a fit of this model to a scan trajectory. This simple model lets us map motion of the piezo scanner to motion of the DNA contour along the pulley. Deviations from Equation (1) indicate the presence of mechanical heterogeneities in the DNA.

Protein bumps on DNA

We tested whether a protein, EcoRI, bound to the DNA introduced a detectable bump in the bead trajectories. EcoRI

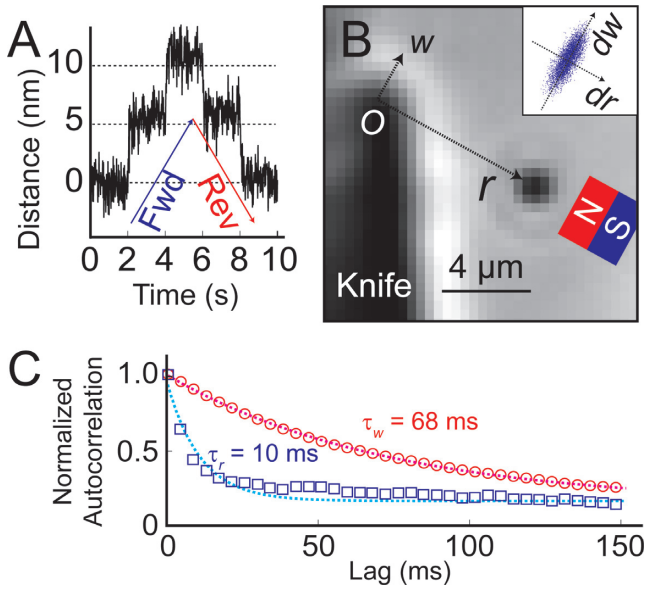

Figure 2. Calibration of the DNA pulley. (**A**) Localization of a bead immobilized on a coverslip. A piezo stage displaced the sample in 5 nm steps. (**B**) Coordinate system for describing bead motion in the DNA pulley. The knife blade is on the left, and a DNA-tethered bead is stretched from the point of contact with the blade toward the magnet (not visible). The origin, *O*, is at the tip of the knife, the *r*-axis is along the direction of magnetic force, and the *w*-axis is orthogonal to the *r*-axis. (Inset) Thermal fluctuations of the tethered bead. The fluctuations were smaller along the *r*-axis (stretching the DNA) than along the *w*-axis (rotation about *O*). (**C**) Normalized autocorrelation functions of the bead displacement. Thermal fluctuations along the *r*-axis decayed faster than along the *w*-axis, as expected for the stiffer spring constant along the *r*-axis. Autocorrelation functions were calculated from 12 000 measurements acquired at 200 Hz.

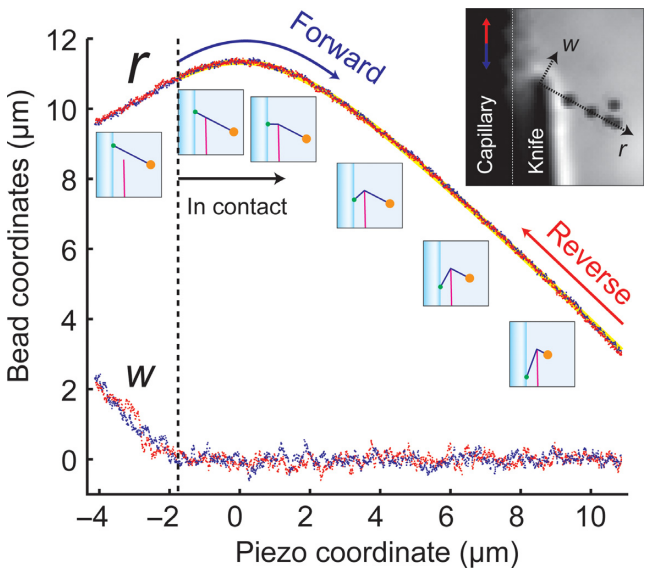

Figure 3. Bead motion in the DNA pulley. The piezo coordinate *p* is positive for downward motion of the capillary. For $P < -2$ mm, the DNA was out of contact with the blade. Initially the *w*- and *r*-coordinates varied with *P* according to their projection along the direction of piezo motion. For -2 mm $< P < 0$ mm, *r* increased as the DNA-capillary junction approached the blade. Thereafter the DNA-capillary junction receded from the blade and the bead was pulled toward the blade. Blue and red points represent measurements of bead location during a forward and reverse scan, respectively. Yellow line represents a fit to Equation (1).

is a type II restriction endonuclease that cleaves its recognition sequence (5′-GAATTC-3′) with high specificity. In the presence of calcium ions, enzymatic cleavage is inhibited without loss of binding activity and specificity, as a result forming stable protein-DNA complexes on specific sites (15). λ-DNA contains five recognition sites for EcoRI spaced ∼2 μm from each other, making this protein a convenient source of sparse bumps.

When the pulley was incubated with EcoRI (50 nM) under non-cleaving conditions (1 mM Ca^{2+} in Tris-HCl buffer, Supplementary Table S2), the bead trajectory showed reproducible pauses at specific locations (Figure 4A and B). The pauses lasted for variable amounts of time before the bead jumped back to the regular trajectory. To test whether these pauses coincided with EcoRI recognition sites, we mapped the scan trajectory onto the underlying DNA sequence. Figure 4C shows the location along the DNA of the blade as inferred from the bead tracking, L_{meas}, versus the location predicted from the motion of the stage L_{pred} (Supplementary Data). Indeed, deviations between the measured and predicted trajectories occurred predominantly when the predicted DNA-blade contact was an EcoRI recognition site.

We explored the region of an EcoRI binding site in greater detail. The blade was scanned repeatedly over a single binding site at 1 μm/s. Bumps in the trajectory were observed in 59/100 forward scans and 73/100 reverse scans (Supplementary Figure S8). The missing bumps likely indicate dissociation of bound protein. Free protein in solution could then re-bind to restore the bump. To estimate the spatial resolution of the DNA pulley system, we calculated the standard deviation of the measured bump location, presuming that the location of the true protein binding site was fixed relative to the DNA. Bump locations had a standard deviation of 85 nucleotides, corresponding to 25 nm.

Remarkably, the distribution of bump durations was very different between forward and reverse scans (Figure 4D, *top*). In the forward direction (bead moving toward blade), bumps were significantly briefer than in the reverse direction (bead moving toward magnet). We interpret this asymmetry by considering the tension in the DNA segment between the capillary and blade (Figure 4D, *bottom*). In the forward direction, pinning of an EcoRI molecule on the blade caused the tension to increase with further displacement of the capillary. In the reverse direction, pinning of an EcoRI molecule on the blade caused the tension to decrease. The shape of the waiting time distribution is quantitatively described by the 'force ramp' model of Evans and Ritchie (16), in which a labile bond is subjected to a tension that grows linearly with time.

We also incubated the pulley in EcoRV, another type II restriction enzyme. The recognition site of EcoRV (5′-GATATC-3′) is present 21 times in λ-DNA. The frequency of asperities increased drastically, with the locations roughly corresponding to the recognition sites. The molecular mapping of EcoRV recognition sites was less reliable than that of EcoRI, possibly due to nonspecific binding of EcoRV to non-canonical sites.

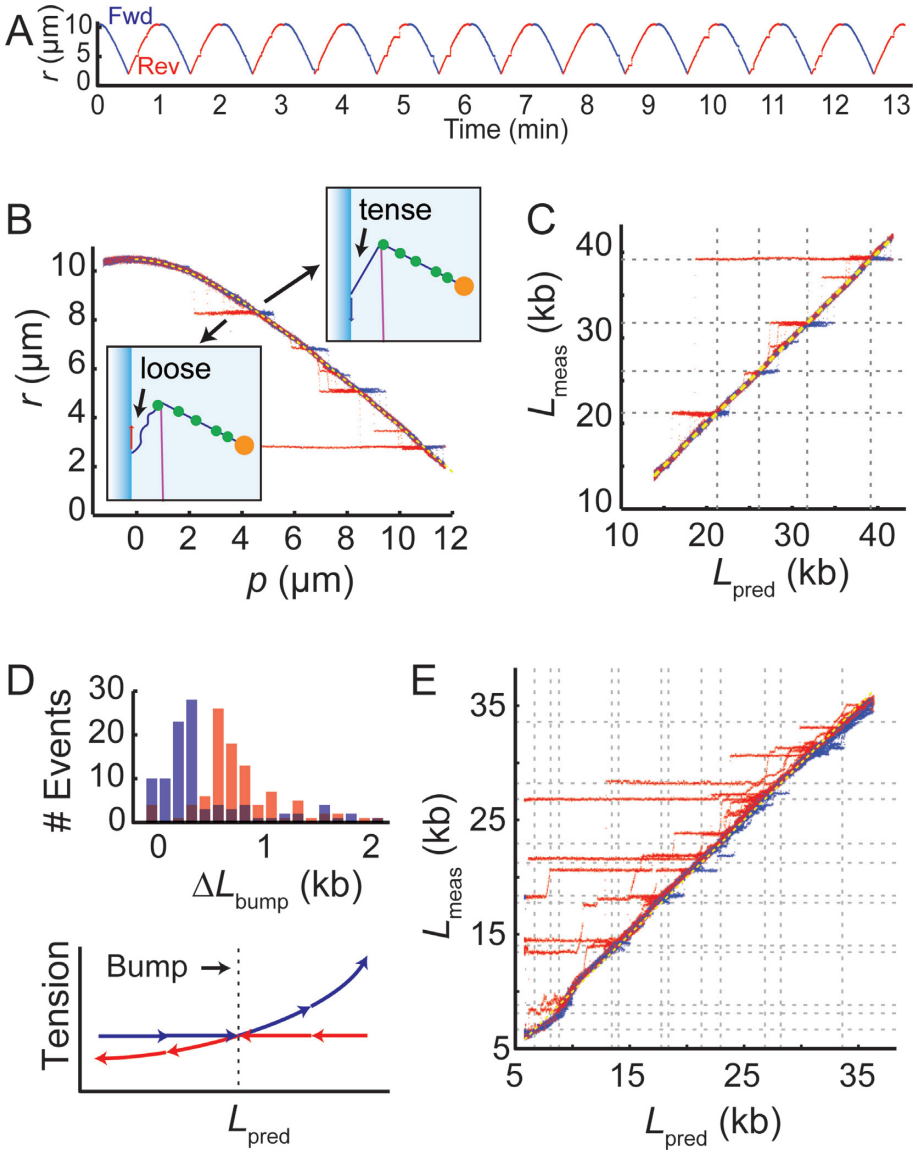

Figure 4. Protein bumps on the DNA pulley. (**A**) Scanning experiments with EcoRI-incubated pulleys revealed reproducible pausing of the bead at specific sites. (**B**) The data in (**A**) were collapsed and plotted as a function of piezo coordinate *p*. The cartoons explain the difference in the induced tension between the forward and reverse scan. (**C**) Mapping of the pause locations onto the EcoRI recognition sites (dashed lines). (**D**) Top: histogram of pause sizes for forward and reverse scans. Here ΔL_{bump} represents the absolute value of change in distance between the capillary-DNA junction and the DNA-blade junction during the interval in which the DNA is stuck (i.e. this would be the amount by which the DNA slid if it were sliding freely). Bottom: cartoon showing tension in the DNA segment between the capillary and the blade, before and after the EcoRI becomes hooked on the blade. In the forward scans, the tension increases after the EcoRI contacts the blade, while in the reverse scans the tension decreases. (**E**) Pauses in a molecule of λ-DNA incubated in EcoRV, mapped onto the EcoRV recognition sites (dashed lines).

Nanomechanics of single-stranded nicks

We next explored whether the DNA pulley could probe the endogenous mechanical properties of DNA itself. We asked whether there were variations in the DNA bending modulus along its length. Alterations to the canonical structure at the base-pair level (e.g. epigenetic modifications, mismatches or damage) modify protein binding and can affect the packaging or looping of DNA. Thus one would like to explore the sequence-dependent mechanical properties of DNA under a range of curvatures and in the presence of the many modifications found in Nature (17–19). These aspects of DNA mechanics have generated controversy in the literature, recently reviewed in detail in references (20,21). Variations in the bending modulus should affect the contour of the DNA around the knife edge, and thereby the displacement of the bead.

We studied the mechanics of a single nick in the phosphodiester backbone. The nick preserves base-stacking interactions, so it does not affect mean flexibility for thermally accessible curvatures (22,23). However, under strong bending a nick facilitates formation of a floppy joint, presumably via disruption of base stacking in the nicked strand (18). We used the enzyme Nb.BbvCI (New England Biolabs), to introduce single-stranded nicks at seven sites in λ-DNA. The

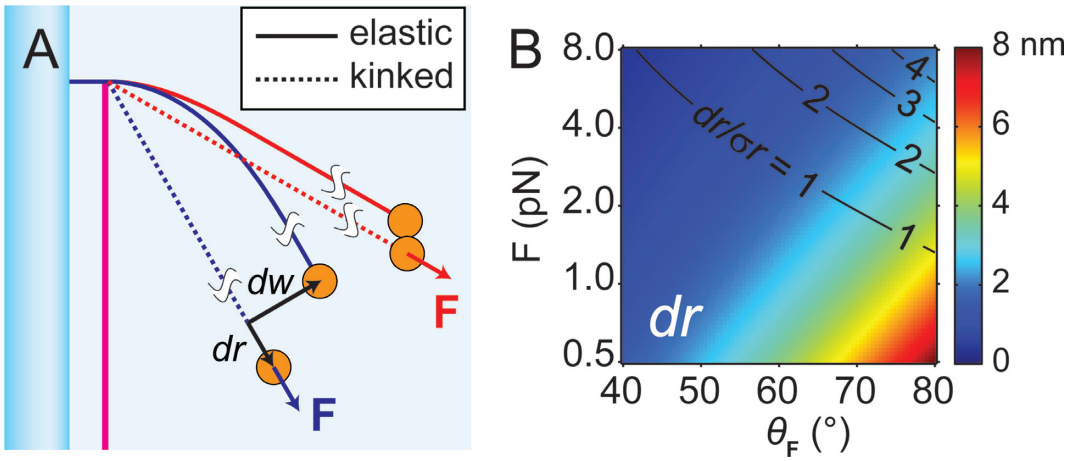

Figure 5. Comparison between kinking and elastica model of DNA bending. (**A**) Cartoon of the DNA pulley comparing the two conformations: elastic bending (solid curve) and kinking (dotted line). The blue and red sets of lines show that the impact of kinking on bead displacements, *dr* and *dw*, depends on the direction of the applied force vector, F. (**B**) Calculation of *dr* for experimentally feasible range of F. |F| is the magnitude of the force, and θ_F is the angle between F and *x*-axis. The ability to resolve length changes *dr* depends on the ratio of *dr* to the amplitude of the thermal fluctuations along $\hat{r}$, σ_r. Black contours indicate lines of constant dr/σ_r.

pulley construct was then incubated in EcoRI under non-cleaving conditions. The molecules of EcoRI served as fiducial marks which helped locate the nick sites. Despite a thorough search at a precision of 25 nm (as determined from the repeatability of localizing EcoRI binding sites), we did not detect any mechanical signature of these nicks (Supplementary Figure S10).

To interpret this result, we calculated the expected bead displacement due to formation of a sharp kink at the blade (Figure 5A). We assumed a perfectly sharp blade (an admittedly crude approximation for a blade whose width is comparable to the persistence length). The mean contour of the smoothly bent DNA is described by a family of mathematical functions known as the elastica (24). In our case the boundary conditions are that the DNA far from the blade must be oriented along the magnetic force, and at the blade the DNA must be perpendicular to the blade edge. In the kinked state, we modeled the DNA as following a straight line from the blade toward the magnet.

Figure 5B shows the expected bead displacement along *r* as a function of the strength and direction of the magnetic force. The displacement is ~2 nm for the 1 pN force and 45° angle range in our experiments. Such a displacement is, in principle, detectable with sufficient signal averaging. We attribute the absence of a detectable signal to the 55 nm width of the blade. The modest curvature around the blade tip may have been insufficient to disrupt base stacking and introduce a kink in the nicked strand. A sharper blade might increase the ability to resolve kinks and other small mechanical heterogeneities.

CONCLUSION

The DNA pulley system provides a facile means to profile the locations of proteins bound to a molecule of DNA, without use of fluorescent labels or optical tweezers. The spatial resolution of the mechanical maps exceeds the diffraction limit. Here we used the DNA pulley to create a detailed mechanical map of the EcoRI binding site. This protocol could be readily adapted to identify previously unknown protein-DNA interaction sites. A key merit of the purely mechanical measurements is that they could be performed in complex media, such as cytoplasmic extracts, without concern for background autofluorescence and without need to fluorescently label putative DNA binding proteins. AFM imaging has been a powerful tool for localizing proteins bound to DNA (5,25–26), although the need for surface immobilization can raise concerns about surface artifacts. The DNA pulley combines spatial resolution of AFM with the ability of magnetic tweezers to apply controlled tension to the molecule.

To probe the endogenous mechanical variability in DNA, the pulley system will require a sharper blade. Extremely thin membranes of silicon nitride can be formed using advanced fabrication techniques. Diamond microtome blades also achieve nearly atomic sharpness. In principle, an appropriately supported graphene sheet could provide the ultimate in spatial resolution. One will need to determine experimentally the limits of applied tension and blade radius of curvature for which the DNA does not break. Finally, functionalization of these blades with DNA-binding proteins or with probe sequences of single-stranded DNA or RNA may provide a means to measure chemically specific interactions with DNA as a function of position along its contour.

SUPPLEMENTARY DATA

Supplementary Data are available at NAR Online.

ACKNOWLEDGEMENT

We thank Alexander Fields for helpful discussions and technical assistance. We thank Xiaowei Zhuang for the loan of a high-precision piezo stage.

FUNDING

National Science Foundation [CHE-0910824]; Dreyfus Teacher Scholar Award; Sloan Foundation Fellowship. Funding for open access charge: Howard Hughes Medical Institute.
Conflict of interest statement. None declared.

REFERENCES

1. Park,P.J. (2009) ChIP–seq: Advantages and challenges of a maturing technology. *Nat. Rev. Genet.*, **10**, 669–680.
2. Gorman,J. and Greene,E.C. (2008) Visualizing one-dimensional diffusion of proteins along DNA. *Nat. Struct. Mol. Biol.*, **15**, 768–774.
3. Collins,B.E., Ye,L.F., Duzdevich,D. and Greene,E.C. (2014) DNA curtains: Novel tools for imaging protein-nucleic acid interactions at the single-molecule level. *Methods Cell Biol.*, **123**, 217–234.
4. Chen,L., Haushalter,K.A., Lieber,C.M. and Verdine,G.L. (2002) Direct visualization of a DNA glycosylase searching for damage. *Chem. Biol.*, **9**, 345–350.
5. Wiggins,P.A., Van Der Heijden,T., Moreno-Herrero,F., Spakowitz,A., Phillips,R., Widom,J., Dekker,C. and Nelson,P.C. (2006) High flexibility of DNA on short length scales probed by atomic force microscopy. *Nat. Nanotech.*, **1**, 137–141.
6. Kowalczyk,S.W., Hall,A.R. and Dekker,C. (2009) Detection of local protein structures along DNA using solid-state nanopores. *Nano Lett.*, **10**, 324–328.
7. Spiering,A., Getfert,S., Sischka,A., Reimann,P. and Anselmetti,D. (2011) Nanopore translocation dynamics of a single DNA-bound protein. *Nano Lett.*, **11**, 2978–2982.
8. De Vlaminck,I., van Loenhout,M.T., Zweifel,L., den Blanken,J., Hooning,K., Hage,S., Kerssemakers,J. and Dekker,C. (2012) Mechanism of homology recognition in DNA recombination from dual-molecule experiments. *Mol. Cell*, **46**, 616–624.
9. van Loenhout,M.T., De Vlaminck,I., Flebus,B., den Blanken,J.F., Zweifel,L.P., Hooning,K.M., Kerssemakers,J.W. and Dekker,C. (2013) Scanning a DNA molecule for bound proteins using hybrid magnetic and optical tweezers. *PLoS One*, **8**, e65329.
10. Han,L., Garcia,H.G., Blumberg,S., Towles,K.B., Beausang,J.F., Nelson,P.C. and Phillips,R. (2009) Concentration and length dependence of DNA looping in transcriptional regulation. *PLoS One*, **4**, e5621.
11. Danilowicz,C., Lee,C.H., Kim,K., Hatch,K., Coljee,V.W., Kleckner,N. and Prentiss,M. (2009) Single molecule detection of direct, homologous, DNA/DNA pairing. *Proc. Natl. Acad. Sci. U.S.A.*, **106**, 19824–19829.
12. Zhou,R., Schlierf,M. and Ha,T. (2010) Chapter sixteen-Force–Fluorescence spectroscopy at the single-molecule level. *Meth. Enzymol.*, **475**, 405–426.
13. Parthasarathy,R. (2012) Rapid, accurate particle tracking by calculation of radial symmetry centers. *Nat. Methods*, **9**, 724–726.
14. Te Velthuis,A.J., Kerssemakers,J.W., Lipfert,J. and Dekker,N.H. (2010) Quantitative guidelines for force calibration through spectral analysis of magnetic tweezers data. *Biophys. J.*, **99**, 1292–1302.
15. McClarin,J.A., Frederick,C.A., Wang,B.C., Greene,P., Boyer,H.W., Grable,J. and Rosenberg,J.M. (1986) Structure of the DNA-eco RI endonuclease recognition complex at 3 A resolution. *Science*, **234**, 1526–1541.
16. Evans,E. and Ritchie,K. (1997) Dynamic strength of molecular adhesion bonds. *Biophys. J.*, **72**, 1541–1555.
17. Geggier,S. and Vologodskii,A. (2010) Sequence dependence of DNA bending rigidity. *Proc. Natl. Acad. Sci. U.S.A.*, **107**, 15421–15426.
18. Fields,A.P., Meyer,E.A. and Cohen,A.E. (2013) Euler buckling and nonlinear kinking of double-stranded DNA. *Nucleic Acids Res.*, **41**, 9881–9890.
19. Du,Q., Kotlyar,A. and Vologodskii,A. (2008) Kinking the double helix by bending deformation. *Nucleic Acids Res.*, **36**, 1120–1128.
20. Vologodskii,A. and Frank-Kamenetskii,M.D. (2013) Strong bending of the DNA double helix. *Nucleic Acids Res.*, **41**, 6785–6792.
21. Peters,J.P. and Maher,L.J. (2010) DNA curvature and flexibility in vitro and in vivo. *Q. Rev. Biophys.*, **43**, 23–63.
22. Shore,D. and Baldwin,R.L. (1983) Energetics of DNA twisting: I. relation between twist and cyclization probability. *J. Mol. Biol.*, **170**, 957–981.
23. Hays,J.B. and Zimm,B.H. (1970) Flexibility and stiffness in nicked DNA. *J. Mol. Biol.*, **48**, 297–317.
24. Landau,L. and Lifshitz,E. (1986) *Theory of Elasticity*. Pergamon Press, Oxford.
25. Lyubchenko,Y.L. and Shlyakhtenko,L.S. (2009) AFM for analysis of structure and dynamics of DNA and protein–DNA complexes. *Methods*, **47**, 206–213.
26. Hamon,L., Pastre,D., Dupaigne,P., Le Breton,C., Le Cam,E. and Pietrement,O. (2007) High-resolution AFM imaging of single-stranded DNA-binding (SSB) protein–DNA complexes. *Nucleic Acids Res.*, **35**, e58.

Supplementary Data

Nano-mechanical measurements on DNA with a silicon nitride pulley

Min Ju Shon[1] and Adam E. Cohen[1,*]

[1] Department of Chemistry and Chemical Biology and [*] Department of Physics, Harvard University, Cambridge, Massachusetts 02138, United States

[*]cohen@chemistry.harvard.edu

Contents

List of Figures

List of Tables

1. Fabrication of the silicon nitride knife

Nanofabrication of the silicon nitride blade

55 nm of low-stress silicon nitride was deposited on a 400 μm-thick (100) silicon wafer using low-pressure chemical vapor deposition (Figure S1). The thickness of the nitride film was measured by ellipsometry. The nitride-coated wafer was hand-diced into 15 mm × 4 mm slivers, briefly rinsed with acetone, cleaned by air plasma for 10 min, and etched in 30% KOH at 75 °C for 20–30 min. A fresh blade was prepared before each experiment.

KOH etching along the straight (111) crystal plane is anisotropic and slow. However, we noticed that when the cleaved wafer had a somewhat curved edge, the etching proceeded much faster (~1 μm/min), possibly by bypassing (111) planes. The etch process left a 15–20 μm silicon nitride overhang. This procedure is robust down to membranes of thickness 30 nm. Below 30 nm, the membrane had a tendency to break upon drying due to surface tension forces.

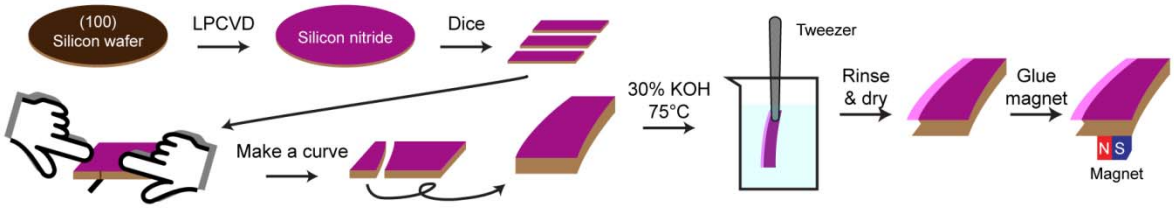

Figure S1. Fabrication of silicon nitride knife. Low-stress silicon nitride film was prepared on a silicon wafer by low-pressure chemical vapor deposition (LPCVD). Silicon under the nitride film was etched by 30% KOH, exposing the nitride blade. The curvature on the edges of the silicon sliver facilitated etching on the sides.

Attachment of magnet to the knife

A 1/16" cubic NdFeB magnet (K&J Magnetics, B111) was glued with epoxy on the back of the knife. The north pole of the magnet was oriented facing the front of the blade. The location of magnet determined the angle and strength of the magnetic force on the pulley, typically pulling the bead with ~1 pN of force at 45° relative to the flat surface of the blade.

2. Preparation of DNA construct

λ-DNA conjugation to bead and surface

λ-DNA (48.5 kb, 16 μm, New England Biolabs) was prepared following a published protocol (1) (Figure S2A) with slight modifications. Circular λ-DNA was dissolved at a concentration of 0.5 mg/mL (15.6 nM) in Tris-HCl buffer with 0.5 M NaCl. The molecule was linearized by heating to 90 °C for 10 min, followed by fast cooling in ice for 5 min. The linearized λ-DNA was then annealed with a 12-nt ssDNA oligo 5' labeled with digoxigenin (dig-12; Integrated DNA Technologies), and complementary to one terminal 12-nt ssDNA overhang (*cos* site). The dig-12 oligo was added at a concentration of 6 nM, selected to be the limiting reagent. The reaction was run for 1 h at room temperature. A second oligo, 5'-labeled with biotin, and complimentary to the other *cos* site, was then added at a concentration of 200 nM and incubated for 1 h at 4 °C. The hierarchy in relative concentrations enabled purification for doubly-labeled λ-DNA by anti-digoxigenin-coated capillaries.

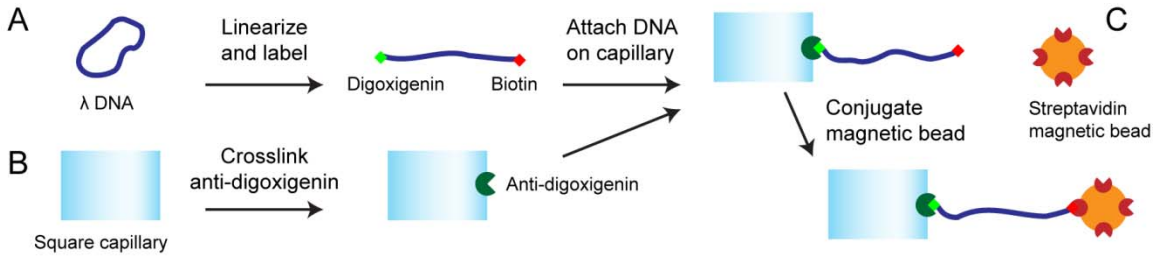

Figure S2. Synthesis of the DNA pulley. (A) A circular form of λ-DNA (blue strand) is linearized and labeled with digoxigenin (green square) and biotin (red square). (B) The exterior of a square capillary is coated with anti-digoxigenin. (C) The capillary with tethered λ-DNAs is labeled with a streptavidin magnetic bead.

Surface attachment of λ-DNA and labeling by magnetic beads

The flat outer surface of square glass capillaries (1 mm I.D., Friedrich & Dimmock, BMC-1-15-50) was used as a substrate for the DNA pulley. These capillaries provided a convenient means to orient the pulley constructs in the focal plane of the microscope. The attachment of λ-DNA (Figure S2B) was adapted from published protocols (2). The sequence of reactions is detailed in Table S1. The aldehyde modification and all subsequent reactions were carried out in PCR tubes (1 capillary per tube) at room temperature. Briefly, the glass surface was activated with glutaraldehyde, amino-modified with APTES, and coated with anti-digoxigenin. The anti-digoxigenin-coated capillary was mixed with labeled λ-DNA. Streptavidin-coated magnetic beads (Dynabeads® MyOne™ Streptavidin C1, Life Technologies, 1 μm diameter, washed following manufacturer's protocol) were then coupled to the DNA on the capillary (Figure S2C). Finally, ligase was added to repair the nicks in the construct (except when nicks were intentional-

ly introduced). Capillaries with attached beads were then transferred to the measurement chamber.

Table S1. Protocol for the synthesis of DNA pulley

Step	Reagent	Duration	Rinse
Capillary cleaning	Acetone Alconox solution (sonication) Air plasma after drying	1 min 10 min 5 min	N/A Water N/A
Amine modification[a]	(3-Aminopropyl)triethoxysilane (Sigma)	4 h	N/A
Aldehyde modification	0.5% Glutaraldehyde (Sigma) in PBS	30 min	PBS
Antibody crosslinking	20 μg/mL Anti-digoxigenin (Roche) in PBS	30 min	WB[b]
DNA tethering	200 pM Biotin- and dig-labeled λ-DNA in PBS	1 h	WB
Surface passivation	WB	15 min	N/A
Bead coupling	4 pM Streptavidin-coated magnetic beads[c] in BB[d]	1 h	WB
Ligation	20 units/μL T4 DNA ligase (New England Biolabs) in T4 DNA ligase reaction buffer	1 h	WB
Bead passivation	50 pM biotinylated oligonucleotides in BB	30 min	PBS
Storage	WB		N/A

[a] Amine modification was carried out in a glass desiccator under vacuum with vapor-phase silane.
[b] WB (wash buffer): 1× TAE buffer with 130 mM KCl, 4 mM $MgCl_2$, 20 μg/mL acetylated bovine serum albumin, 80 μg/mL heparin.
[c] Streptavidin-coated beads (Dynabeads® MyOne™ Streptavidin C1, Life Technologies) were rinsed before use following manufacturer's protocol.
[d] BB (binding buffer): WB with 1 M NaCl

3. Measurement setup

Sample chamber and stages

A capillary with DNA pulley was mounted in a custom Teflon/aluminum chamber with a glass bottom for imaging (Figure 1F in the main text). The chamber was loaded with 500 µL of sample solution and mounted on a nanopositioning piezo stage (Mad City Labs, Nano-LP100). The piezo stage was mounted on a manual micropositioning stage (Mad City Labs, MicroStage) for coarse positioning. The silicon nitride knife was clamped on a separate *xyz*-micromanipulator (Newport) and was aligned relative to the capillary. The knife-edge was aligned orthogonal to the *x*-*y* plane to avoid out-of-plane movements in the bead during the scanning.

The entire setup including the microscope was enclosed in a box to block air currents and supported on a vibration-isolation optical table. Shielding of air currents was essential to obtaining low drift: without the shield, drift was ~10 nm/min, and with the shield, drift was ~1 nm/min.

Optical setup

Measurements were performed on an inverted microscope (Olympus IX71). The sample was illuminated from above with a white LED. The image of the magnetic bead, silicon nitride knife, and capillary was collected with a 40× air objective (Olympus, N.A. 0.60), passed through a 3× beam expander, and recorded with an EMCCD camera (Andor DU-897-UV, 16-µm pixels), operated without electron-multiplying gain. Frame rates were selected between 2 and 200 Hz depending on the measurement.

Composition of sample buffer

For all DNA pulley experiments, we used the following Tris-HCl buffer. 1 mM of $CaCl_2$ was added for experiments with EcoRI/EcoRV.

Table S2. Composition of scanning buffer

Materials	Concentration
Tris-HCl (pH 8.0)	10 mM
NaCl	100 mM
Polyvinylpyrrolidone	0.1%
Tween-20	0.1%

4. Localization of fixed beads

Bead-to-bead distance measurements

To estimate the precision of bead localization we imaged two beads fixed on a glass coverslip. The beads were tightly fixed on the surface, so apparent fluctuations in bead-to-bead distance arose purely from measurement error. The position of the coverslip was advanced in 5 nm steps and imaged with an exposure time of 20 ms. Movies were averaged over 1 s and the bead coordinates were extracted by a radial symmetry-based algorithm on 15×15 pixels region of interest.(3)

Regardless of the underlying movement of the piezo stage, the measured distance between the two beads was nearly constant, showing tight correlation in the movements (Figure S3). The fluctuation in the inter-bead distance, σ_d, measured at 1 Hz was 1.9 Å. The measurement of inter-bead separation involves two measurements of position, each associated with the same measurement error, so the precision of localization for a single bead is $1.9/\sqrt{2}$ = 1.3 Å in a 1 Hz bandwidth.

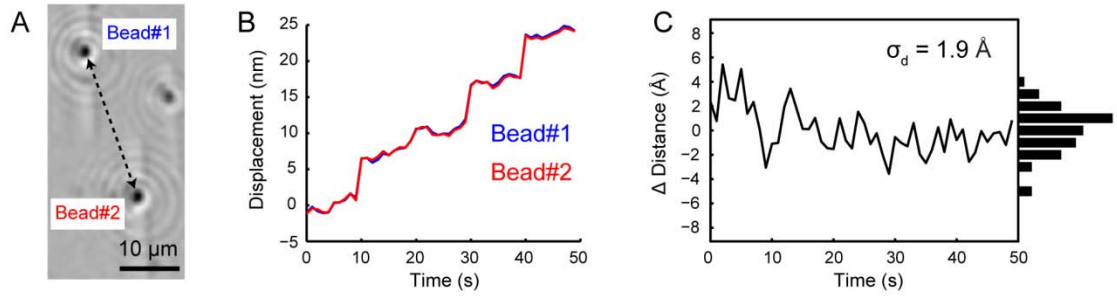

Figure S3. Precision of bead localization. (A) Two beads were fixed on a dry coverslip and imaged as a piexo stage moved the sample. The localization precision was inferred from the measurement error in the inter-bead distance (black dashed line). (B) Displacement of the two beads over time. The beads were moved by piezo stage with 5 nm steps. (C) Bead-to-bead distance over time.

Calibration of piezoelectric stage

The precision of the piezoelectric stage (Mad City Labs, Nano-LP100) was measured by following 5 nm steps over a total displacement of 1 μm. As shown in Figure S4, the motion of piezo stage introduced 2-nm r.m.s. mechanical noise in an 1 Hz bandwidth.

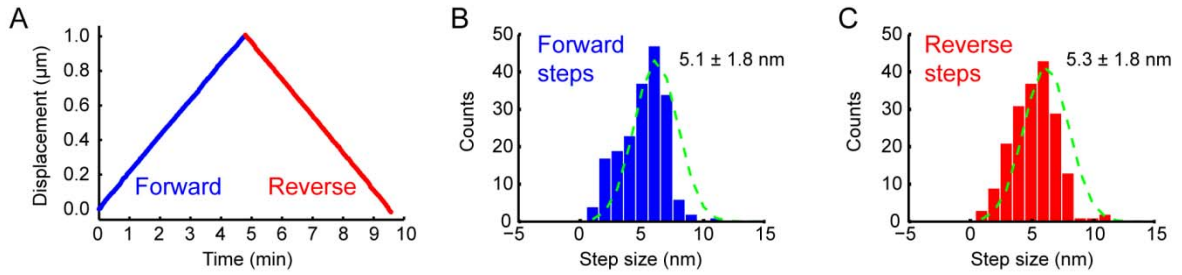

Figure S4. Calibration of piezoelectric stage. (A) Tracking 5 nm steps in a ramp of 1 μm total displacement. Forward (blue) and reverse (red) travel. (B–C) Distribution of step sizes for forward (B) and reverse (C) steps.

Long-term drift

The level of mechanical drift was checked by tracking a bead over many hours. As shown in Figure S5, the length-scale of mechanical drift was ~1 nm in 1 min, and ~10 nm in 1 h. Characterization of noise by Allan variance (4) showed a gradual increase of deviation over long time-scales due to the drift (Figure S5D).

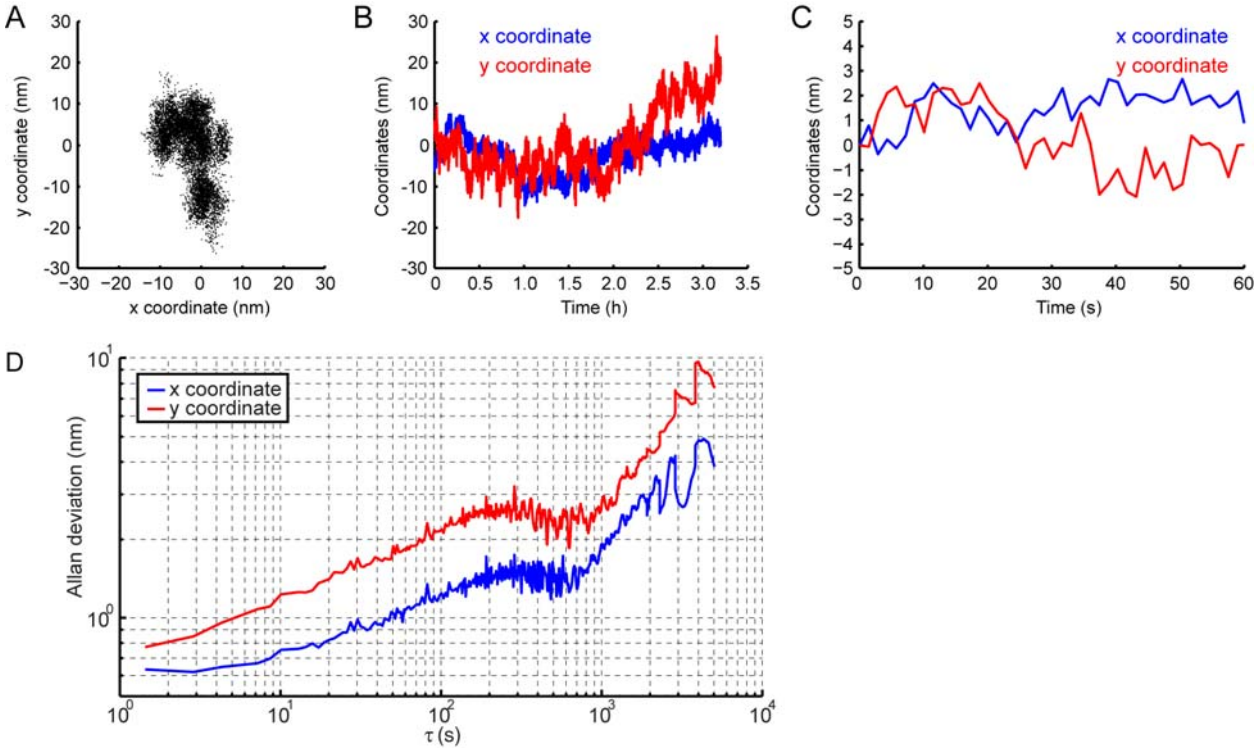

Figure S5. Long-term mechanical drift. Tracking of a nominally stationary bead at 1.4 s intervals for 3.2 hr. (A) 2-D distribution of measured bead locations. Each point represents one measurement. (B) *x*- and *y*-coordinates as a function of time. The low-frequency drift is ~10 nm/hr. (C) The drift on short time scale is ~1 nm/min. (D) Allan deviation of the x (blue) and y (red) coordinates for the data in (B).

5. Calibration of magnetic force on the pulley

Fluctuation measurement

A bead on a spring undergoes thermal fluctuations of mean square amplitude along each axis:

$$\sigma^2 = \frac{k_B T}{k} \quad (1)$$

where k is the spring constant, k_B is Boltzmann's constant and T is the absolute temperature. These fluctuations decay with a correlation time:

$$\tau = \frac{\gamma}{k} = \frac{6\pi\eta a}{k} \quad (2)$$

where γ is the drag constant, η is the dynamic viscosity of the medium, a is the radius of the bead.

The effective spring constants along the *r*- and *w*-axes are in turn related to the magnetic force. Along the *r*-axis, the force and extension are related by the modified Marko-Siggia formula for a WLC (5) :

$$F = \left(\frac{k_B T}{l_p}\right)\left[\frac{1}{4(1 - x/L_0)^2} - \frac{1}{4} + \frac{x}{L_0}\right] \quad (3)$$

where F is the force; x is the extension; l_p = 45 nm is the persistence length; L_0 = 16.2 μm is the contour length; and K_0 = 1000 pN is the elastic modulus (6). The effective spring constant is:

$$k_r = \left.\frac{dF}{dx}\right|_{x=r} \quad (4)$$

The magnetic force on the bead was measured from thermal fluctuation of the bead, *in situ* before scanning experiments (Figure S6). The bead fluctuation with all stages at rest and with the blade withdrawn was recorded at 200 Hz.

To quantify the bias induced by the finite exposure time of the camera, we ran a simple numerical simulation of a Brownian particle in a harmonic potential with a 10 ms relaxation time. We used 0.1 ms time-steps and produced a trajectory of 10^6 steps. We then simulated the effect of the finite exposure time of the camera by averaging the trajectory in 5 ms discrete intervals. The autocorrelation functions of the raw and discretely sampled trajectories are shown in Figure S6D. Discrete sampling led to an underestimate of the variance in particle position by 17%, but a negligible influence on the autocorrelation function at non-zero lag. For motion of a particle with a correlation time of 70 ms, discrete sampling with 5 ms integration times led to an underestimate of position variance of only 2.5%.

To fit the autocorrelation functions, we discarded the data point at zero lag (on account of the bias from finite camera exposure). We then fit the remaining data to a function of the form A $\exp(-t/\tau)$ + B. The purpose of the constant offset, B, was to accommodate slow drift in the measured bead position, which led to a plateau in the autocorrelation function at timescales long com-

pared to the relaxation time. Typical time scales of fluctuations were τ_r ~10 ms along *r*, and τ_w ~70 ms along *w* (Figure S6B and C).

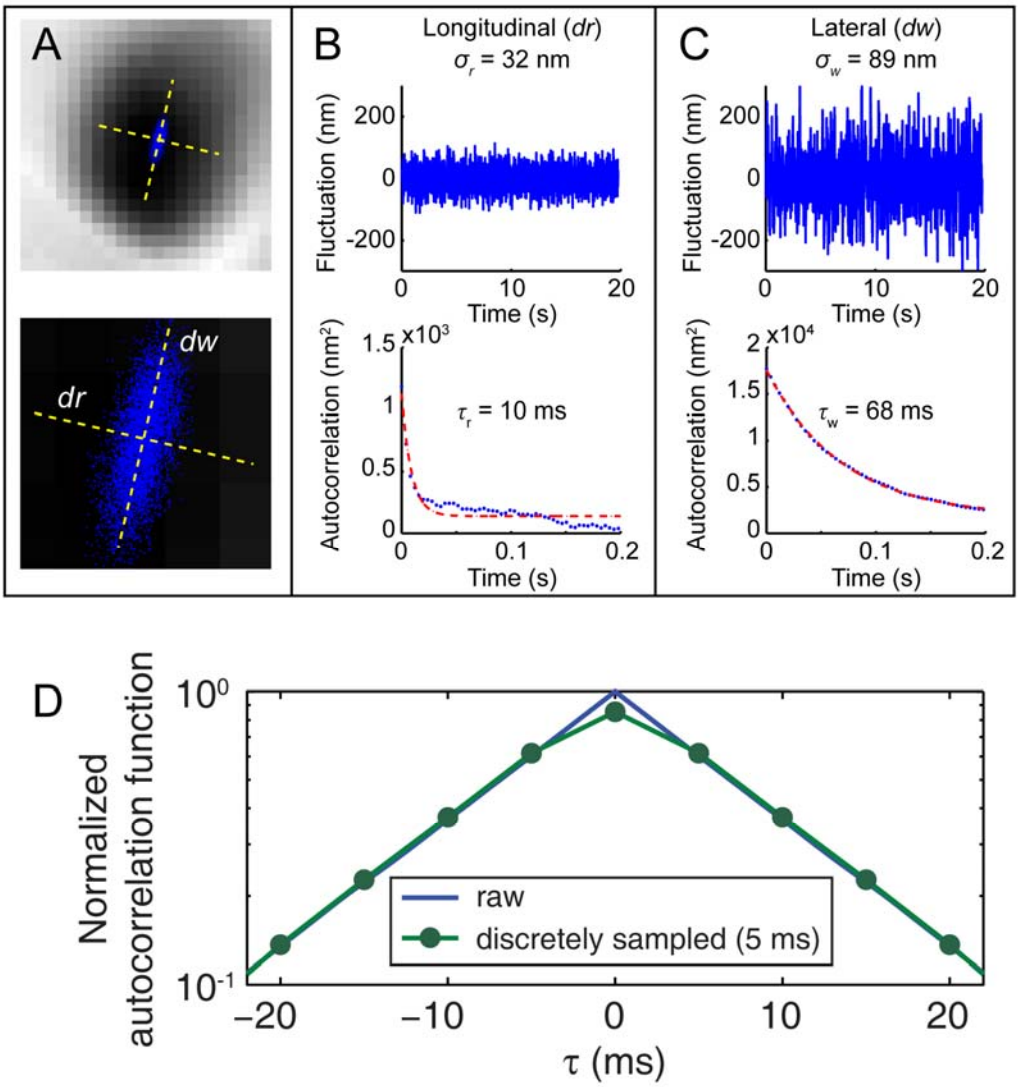

Figure S6. Thermal fluctuations of a tethered bead. (A) Image of fluctuating bead, recorded at 250 Hz and averaged for 1 min. Blue dots are the bead localization for each frame. Yellow dashed lines indicate the axes extracted from the principal axes of the ellipse of points. Bottom image is a close-up view of the distribution of points. (B) Fluctuation along the *r*-axis and autocorrelation of these fluctuations (bottom). (C) Fluctuations along the *w*-axis and autocorrelation of these fluctuations. (D) Effect of finite exposure time of camera on the autocorrelation function of Brownian trajectory. The autocorrelation function for the raw trajectory of simulated Brownian motion (blue without marker) was compared with that for the same trajectory after averaging and then discrete sampling with a 5 ms window.

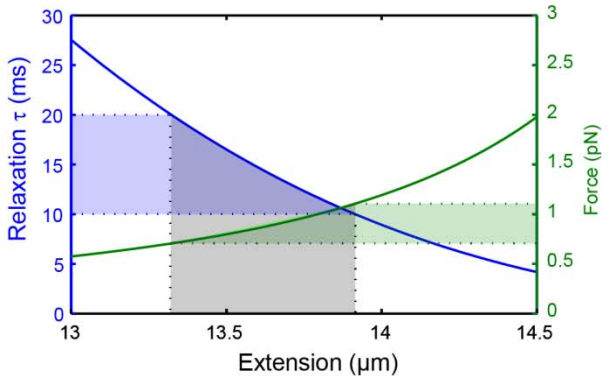

Figure S7. Calibration of force on the DNA pulley. (*Left y-axis*) Measured relaxation time of the bead fluctuations. (*Right y-axis*) Stretching force on the DNA. The relaxation time ranged from 10 to 20 ms. These values correspond to, by Eq. **(9)**, 13–14 μm extension of λ-DNA (85% extension) and ~1 pN of magnetic force.

6. Localization of protein-DNA complexes

Incubation with restriction enzymes

The DNA pulley was first incubated with 50 nM EcoRI-HF or EcoRV-HF (New England Biolabs, R3101 and R3195) in a scanning buffer (Table S2) containing 1 mM $CaCl_2$ (10 mM Tris-HCl, 100 mM NaCl, 0.1% polyvinylpyrrolidone, 0.1% Tween-20), for 1 h. After incubation, the number of pulley constructs on capillary was not reduced substantially, confirming that the catalytic activity of the restriction enzymes was lost.

The EcoRI-incubated DNA pulley constructs were studied by applying the same scanning condition as in the simple trajectory mapping. The scanning speed was 1 μm/s with a 100 Hz camera frame rate.

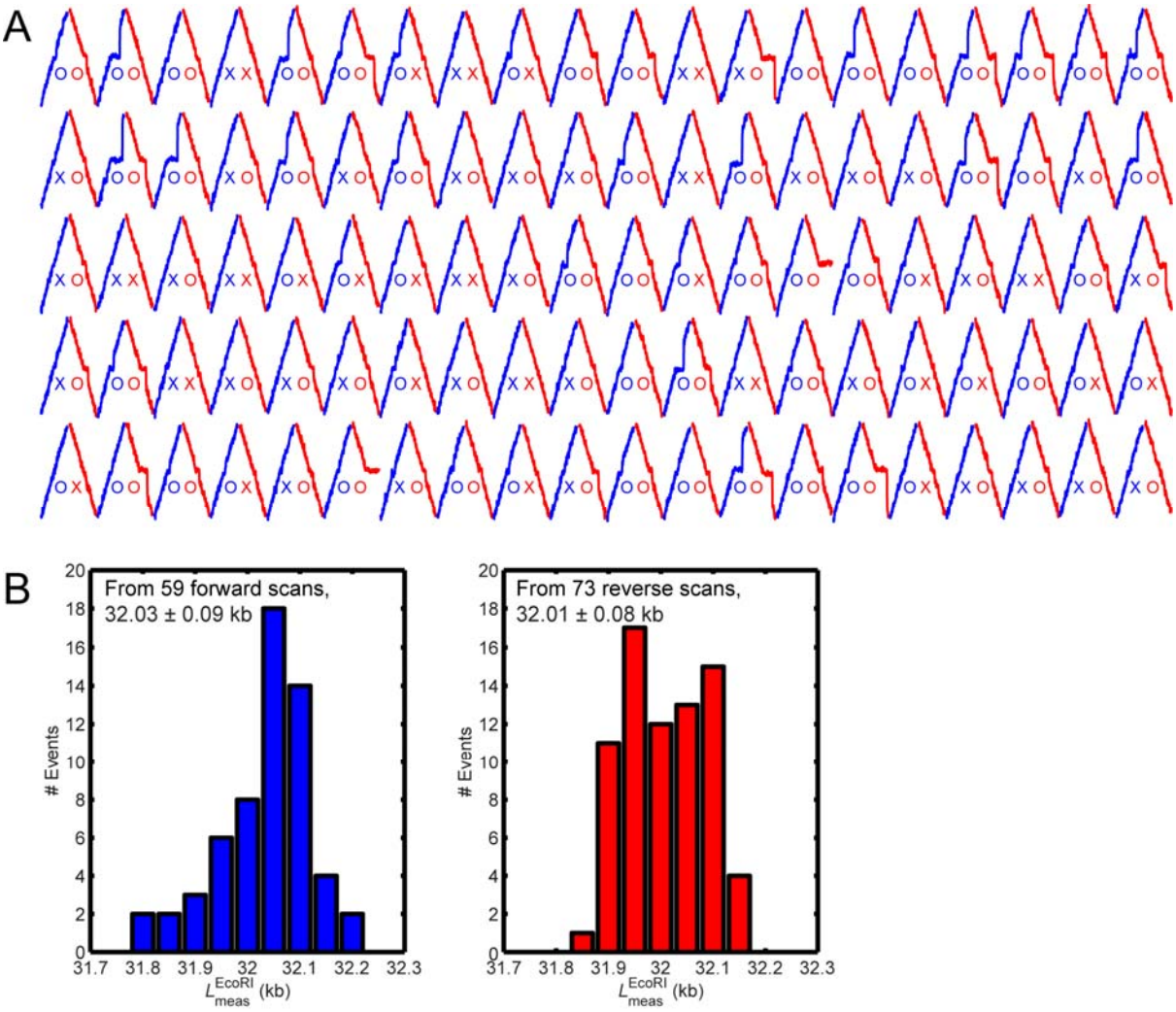

Figure S8. Repeated detection of protein bumps on the DNA pulley. (A) 100 consecutive forward (blue) and reverse (red) scans. EcoRI bumps were detected as deviations from the predicted bead trajectory. Bumps were detected in 59 forward scans and 73 reverse scans (denoted as "O"). (B) Histograms for the locations of EcoRI bumps detected in (A). The standard deviation in bump location in either direction was ~25 nm.

7. Converting bead displacements to molecular coordinates for molecular mapping

Geometry of the DNA pulley

We solved the geometry of the pulley system to parameterize the bead motion. We then mapped the measured bead coordinate, *r*, onto the location in the DNA sequence of the DNA-blade contact.

The analysis of the pulley geometry is greatly simplified if the blade edge is aligned parallel to the *z*-axis. Before experiments, the microscope focus was moved along the *z*-axis and the blade edge was aligned to be vertical. However, the angle of the magnetic force vector is not precisely controlled due to the need to manually position the magnet prior to gluing. Furthermore, the similar scale of the magnet size (1/16") and the distance between the magnet and the bead implies that the magnetic field contour at the bead location is not simple to compute. The angle of the magnetic force in the *x*-*y* plane is trivially determined by noting the direction of DNA stretching; but the azimuthal angle, $\phi_{\mathbf{F}}$, relative to the *z*-axis must be included as a fitting parameter.

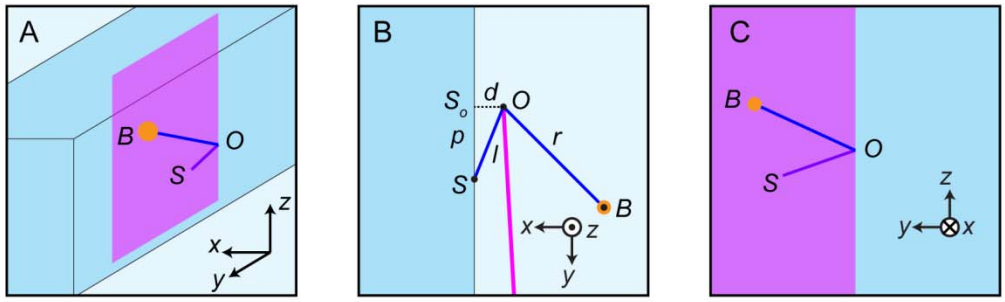

Figure S9. Geometry of the DNA pulley. (A) 3-D view of the pulley system. The points *B*, *O*, and *S* are the coordinates for the bead, pivot on the blade (origin), and surface attachment point, respectively. (B) The pulley viewed in the *x*-*y* plane, corresponding to the image plane of the microscope. (C) The pulley viewed in the *y*-*z* plane. Note that the three points *B*, *O*, and *S* do not lie in the *x*-*y* plane when $\phi_{\mathbf{F}} \neq \pi/2$, where $\phi_{\mathbf{F}}$ is the azimuthal angle of the force vector (measured relative to the *z*-axis). The apparent contour length observed in the microscope, l_0, is the projection onto the *x*-*y* plane of the true contour length L_0. Thus $l_0 = L_0 \sin(\phi_{\mathbf{F}})$.

When the *z*-component of the magnetic force vector is not zero, the bead is pulled out of the *x*-*y* plane, and therefore the *z*-coordinates of the three points *B* (bead), *O* (pivot or origin), and *S* (surface attachment) can be different (Figure S9). The focus of the microscope is adjusted so that only *B* is located in the image plane. Translation of the capillary (and hence *S*) along the *y*-axis does not change the *z*-coordinate of *B*, i.e. the bead remains in the focal plane during the scanning process, regardless of a vertical offset in the stretching force.

From Figure S9B, we can relate the observed bead coordinate, *r*, to the piezo coordinate, *p*. Let *d* be the distance between the capillary and the knife, and let S_0 be the position on the capillary closest to the knife edge. The DNA-capillary attachment is inferred to cross S_0 when the DNA appears maximally extended along *r*. This piezo coordinate is defined as $p = 0$.

From the right triangle $\triangle SS_0O$, we get

$$l^2 = p^2 + d^2. \tag{5}$$

Therefore, the extension of the DNA between *O* and *B*, *r*, is given by

$$r = l_0 - l = l_0 - \sqrt{p^2 + d^2} \tag{6}$$

where l_0 is the total extension of DNA projected onto the *x*-*y* plane. Note that l_0 is always shorter than the total contour length L_0 (16.2 μm) because: (a) the DNA is not fully extended by the stretching force, and (b) the *z*-component of magnetic force might be nonzero, pulling the molecule slightly out of the *x*-*y* plane.

Ratiometric measurements of length and molecular coordinate

The relation of the observed contour length projected into the *x*-*y* plane, l_0, and the total extension in 3-D, L_0, is

$$l_0 = L_0 \sin \phi_{\mathbf{F}} \tag{7}$$

where $\phi_{\mathbf{F}}$ is the azimuthal angle of the magnetic force vector. In our measurements, the two variables, L_0 and $\sin \phi_{\mathbf{F}}$ do not have to be separated. Hence we regard l_0 as a single fitting parameter, acknowledging that we do not know L_0 and $\sin \phi_{\mathbf{F}}$ independently. The progression of the blade relative to the molecule in the image plane, l/l_0, is the same as the one in 3-D space, L/L_0. Therefore, knowledge of the ratio l/l_0 is sufficient to infer the absolute position, i.e., the sequence coordinate of the DNA-blade contact.

Deviations from pure pulley motion due to protein bumps on the DNA

When a DNA-bound protein catches on the blade edge, the measured location of the bead deviates from the predicted location, and therefore the point of contact between the DNA and blade as inferred from bead tracking deviates from the point of contact predicted from piezo motion. From Eq. (6), the predicted location of blade, $L_{\mathrm{pred}}(p)$, is:

$$L_{\mathrm{pred}}(p) = \left(\frac{\sqrt{p^2 + d^2}}{l_0}\right) \times (48.5 \text{ kb}). \tag{8}$$

The blade position inferred from bead tracking is:

$$L_{\mathrm{meas}}(p) = \left(\frac{l_0 - r}{l_0}\right) \times (48.5 \text{ kb}) \tag{9}$$

In the absence of bumps along the DNA, the measured position of the blade $L_{\mathrm{meas}}(p)$ will be the same as prediction, $L_{\mathrm{pred}}(p)$. By comparing L_{meas} to L_{pred}, deviation from regular trajectory can be followed as a function of sequence.

8. Measurement of DNA bending around a single-stranded nick

The capillary with appended DNA and beads was incubated with Nb.BbvCI at 37 °C for 1 h for nicking. The capillary was then washed with WB (Table S2) to remove nicking enzymes. The sample was then incubated with EcoRI, as in Section 6.

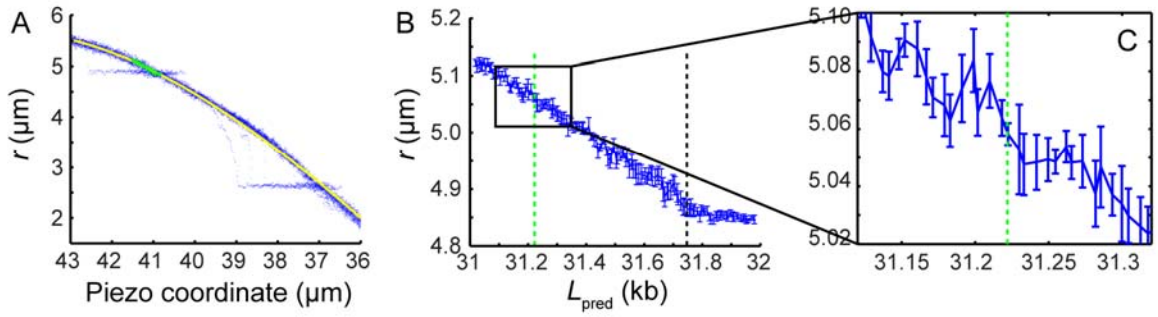

Figure S10. Measurement of DNA bending around a single-stranded nick. (A) Scans encompassing two EcoRI binding sites. The highlighted segment (upper left, green) includes an EcoRI site located close to a recognition site for the nicking enzyme Nb.BbvCI. (B) Slow scans around the highlited region in (A). Black and green lines indicate sites for EcoRI and Nb.BbvCI, respectively. Error bars indicate standard errors calculated from 7 measurements. (C) Close-up of (B) near the putative nicking site.

9. Simulation of DNA bending using theory of elastica

A sharp kink, i.e. a region of perfect flexibility, constitutes the largest mechanical signal one might hope to detect in DNA, and could arise e.g. from a single-stranded nick, a bubble, or possibly from covalent damage to the DNA. We thus sought to estimate the deviation in bead coordinate that would be induced by a running a point of perfect flexibility over the blade, assuming a perfectly sharp blade.

We compare the bead position under two scenarios: (1) the DNA bends smoothly around the edge of the (assumed perfectly sharp) blade, following the contour set by the applied tension and the continuum elasticity of the DNA; and (2) the DNA adopts a sharp kink at the blade and then extends in a straight line along the magnetic force. This calculation constitutes an upper bound on the signal. The blades used in our experiments were not sharp (55 nm diameter of curvature) compared to the persistence length, so our experiments would yield signals smaller than the estimates below.

For radii of curvature much smaller than the persistence length, the contour of a homogeneous linear elastic rod is described by a set of curves called the elastica. We modeled DNA as a simple elastic rod experiencing an external force on the ends. Due to the two-fold mirror symmetry of the force in the DNA pulley, we only consider the half with a magnetic bead.

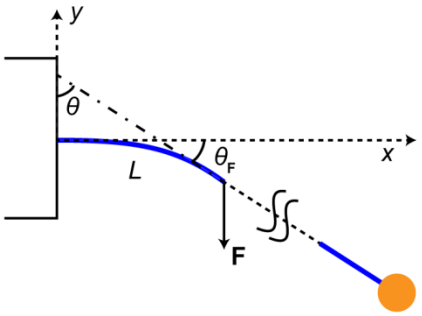

Figure S11. Elastica model for the bending of DNA.

The bending of DNA pivoted on the nitride blade can be thought of as a rod with one end clamped (Figure S11). Consider a segment of the tethered DNA with a length L, smaller than the persistence length (50 nm). The distal end of this DNA segment is pulled along the direction of magnetic tension. The angle between the tangent to the rod and the y-axis (θ) is related to the force and the rod length by (7):

$$L = \sqrt{\kappa/(2\mathrm{F})} \int_{\theta_0}^{\pi/2} \frac{cos\,\theta\, d\theta}{\sqrt{cos\,\theta_0 - cos\,\theta}} \qquad (10)$$

where κ is the bending modulus and $\mathrm{F} = |\mathbf{F}|$ is the applied force. The direction of magnetic force sets a boundary condition for the slope of curve. We solve for an elastica that asymptotes to the force angle ($\theta_0 = \pi/2 - \theta_\mathbf{F}$). Substituting $\theta_\mathbf{F}$ into the Eq. (10) gives a length scale, L^*, over

which the DNA transitions from a bent to a linear shape. The complete shape of the elastica regime (Figure S12, solid curves) is parametrically given by $\theta_{\mathbf{F}}$:

$$x = \sqrt{2\kappa/\mathrm{F}}\left[\sqrt{cos\,\theta_{\mathbf{F}}} - \sqrt{cos\,\theta_{\mathbf{F}} - cos\,\theta}\right],$$
$$y = \sqrt{\kappa/(2\mathrm{F})}\int_{\theta}^{\pi/2} \frac{\cos\theta\, d\theta}{\sqrt{\cos\theta_{\mathbf{F}} - \cos\theta}}. \qquad (11)$$

As depicted in Figure S12A and B, the signal we are looking for is the difference in the bead position, resulting from a change in the local structure. If the DNA behaves as a perfect WLC, it will follow the solid curves. If the curvature introduced in the DNA is relieved by a localized kink, it follows a free-joint curve shown in dashed lines. To estimate the signal, the coordinates of the end of the DNA segment are compared for the two models.

A large force angle or a weak force is expected to give a large difference between the smoothly bent and the kinked state. The amplitude of the lateral displacement, *dw* is generally larger than the radial displacement, *dr* (Figure S12C and D).

One must compare the amplitudes of the displacements to the amplitudes and timescales of the thermal fluctuations in bead position. Thermal fluctuations are larger and slower for a weak force than for a strong force; and are larger and slower for measuring *dw* than for measuring *dr*. To detect kinks or other intrinsic mechanical heterogeneities in DNA will require (a) a sharper blade than we used, and (b) better long-term stability of the apparatus to permit averaging the bead coordinate over many relaxation time constants to achieve better tracking accuracy.

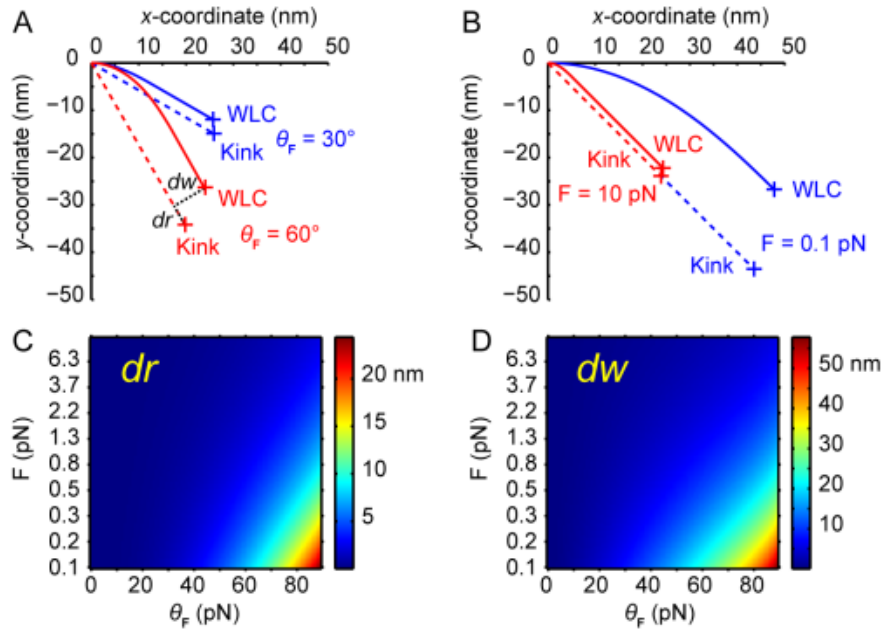

Figure S12. Calculation of DNA bending comparing elastica and kinked DNA. DNA is modeled as a rod with a persistence length 46.5 nm (solid curves) and compared to the kinked model (dashed lines). Crosses on the curves are marked keeping the contour lengths the same for the two cases. (A) Varying the force angle, $\theta_{\mathbf{F}}$, at a constant force magnitude F = 1 pN. The difference between the elastic and kinked model is greater at a larger angle. The longitudinal and lateral difference is designated as *dr* and *dw*,

respectively. (B) Varying the force magnitude, F, at a constant force angle $\theta_{\mathbf{F}} = 45°$. The difference between the elastic and kinked model is greater at a smaller force. (C–D) Extended simulations of the plots in (A) and (B).

10. References

1. Zhou,R., Schlierf,M. and Ha,T. (2010) Chapter sixteen-Force–Fluorescence spectroscopy at the single-molecule level. *Meth. Enzymol.,* **475,** 405-426.

2. Han,L., Garcia,H.G., Blumberg,S., Towles,K.B., Beausang,J.F., Nelson,P.C. and Phillips,R. (2009) Concentration and length dependence of DNA looping in transcriptional regulation. *PLoS One,* **4,** e5621.

3. Parthasarathy,R. (2012) Rapid, accurate particle tracking by calculation of radial symmetry centers. *Nat. Methods,* **9,** 724-726.

4. Czerwinski,F., Richardson,A.C. and Oddershede,L.B. (2009) Quantifying noise in optical tweezers by allan variance. *Optics Express,* **17,** 13255-13269.

5. Marko,J.F. and Siggia,E.D. (1995) Stretching DNA. *Macromolecules,* **28,** 8759-8770.

6. Wang,M.D., Yin,H., Landick,R., Gelles,J. and Block,S.M. (1997) Stretching DNA with optical tweezers. *Biophys. J.,* **72,** 1335-1346.

7. Landau,L. and Lifshitz,E. (1986) Theory of Elasticity. Pergamon Press, Oxford, UK.